IEEE Access
Multidisciplinary | Rapid Review | Open Access Journal

Received December 10, 2020, accepted December 13, 2020, date of publication December 16, 2020,
date of current version December 30, 2020.

Digital Object Identifier 10.1109/ACCESS.2020.3045142

Reconfigurable Frequency Selective Rasorber Covering Extremely Wide Transmission Frequency Range

JING TIAN, BO CHEN, (Member, IEEE), BIXIAO JIANG, RUIMING LI, (Student Member, IEEE), SHIWEN LEI, (Member, IEEE), AND HAOQUAN HU

University of Electronic Science and Technology of China, Chengdu 611731, China

Corresponding author: Bo Chen (chenbo@uestc.edu.cn)

This work was supported in part by the National Natural Science Foundation of China under Grant 62001095 and Grant U20B2043, and in part by the Fundamental Research Funds for the Central Universities of China under Grant ZYGX2018KYQD200.

ABSTRACT Rasorbers with reconfigurable transmission frequency are of great interest over the past few years. However, existing devices exhibit a limited number of operation modes and cover a narrow transmission frequency range, making them unacceptable for wideband applications. In this work, a high-performance reconfigurable rasorber with mechanically-controlled frequency selective surface (FSS) and an electronically-tuned resistive layer is proposed. Theoretical analysis based on transmission line theory and numerical simulations is performed to investigate the performance of the proposed device. The rasorber were fabricated and free-space measurements were also carried out to validate the simulation results. The device can operate between single-, dual- and triple-passband modes by mechanically tuning the FSS under a fixed external bias voltage. Under single-passband mode, the transmission frequency can also be tuned continuously through simultaneously controlling the mechanically-tunable FSS and electronically-tunable resistive layer. A minimum insertion loss as low as 0.16 dB at 4.03 GHz is achieved from the measurement results. The maximum measured fractional absorption bandwidth is 87.9%, comparable to the state-of-art maximum absorption bandwidth of existing reconfigurable rasorber. The measured overall fractional transmission frequency range under normal incidence wave is 63.9%, far beyond that of any other existing reconfigurable counterparts.

INDEX TERMS Reconfigurable, rasorber, mechanical, electronic.

I. INTRODUCTION

Electromagnetic (EM) frequency selective rasorber is an artificial material or device that allows EM waves propagate through nearly losslessly within its transmission band while absorbs EM waves at other frequency bands. The early attempt of utilizing periodic metamaterial structure to realize EM rasorbers have been conceptually introduced by B. A. Munk [1]. Later on, a couple of EM rasorbers with detailed theoretical analysis and experimental validation have been reported [2]–[25]. In terms of physical geometry, the existing rasorbers can be divide into lateral (or 2D) and 3D devices. Generally, a 2D EM rasorber consists of a 2D resistive layer on top and a 2D frequency selective surface (FSS) underneath. A quarter wavelength air gap between resistive layer and FSS is usually required in lateral devices [2]–[17] while their 3D counterparts are based on parallel-plate waveguide structures with subwavelength thickness [18]–[25]. The advantages of 3D rasorber compared with the lateral ones include broad transmission bandwidth, improved selectivity and stability under oblique incidence. However, due to the structural complexity of 3D rasorbers, most of the reported experimental investigations have been concentrated on 2D devices.

Experimental explorations of rasorbers with single absorption and transmission band were firstly reported in the early ages [2]–[7]. Those exhibit an absorption band at lower frequency and a transmission band at higher frequency are

The associate editor coordinating the review of this manuscript and approving it for publication was Kwok L. Chung.

classified as A-T rasorbers, where A stands for absorption and T means transmission. The T-A rasorbers, on the contrary, hold a higher absorption band and lower transmission band. Later, a series of scenarios with dual absorption bands locating on both sides of the transmission window (i.e. A-T-A type) were also presented [8]–[17]. In addition, rasorbers with dual transmission bands were also experimentally investigated by M. Guo *et al.* [26], [27]. Compared with the A-T and T-A types with a single transition region between transmission and absorption bands, the A-T-A or dual-band rasorbers exhibit more transition bands with unacceptable absorption or transmission performance. To reduce the width of transition bands, X. Xiu *et al.* utilized high-order FSS to improve the selectivity of the transmission band for their A-T-A rasorber [15]. However, the resultant narrow transmission band is not favored in broadband applications. Although high-order FSS has also been used in rasorber design to achieve broad transmission bandwidth and fast roll-off characteristic [25], [28], the reciprocity of EM wave transmission within the passband degrades its stealth performance.

One potential solution to this constriction is to use PIN diodes as switches to turn off the transmission window when necessary [12], [29]. Hence, in the off-state both transmission and transition bands are eliminated and a single absorption band can be achieved over an ultra broad frequency of interest. However, the reported switchable rasorbers exhibit a relatively narrow transmission band compared with those exhibiting fixed absorption and transmission performance. Alternatively, the rasorbers with a narrow but tunable passband can also be used to extend the overall effective transmission frequency range. In addition, reconfigurable rasorbers are also suitable to be used as the radome materials for the radar cross section (RCS) reduction of reconfigurable antennas within its absorption band. In early 2019, L. Wu *et al.* reported a tunable A-T-A rasorber with fast roll-off characteristics on both sides of the passband [30]. However, the minimum insertion loss as high as 3.3 dB makes it unacceptable for practical applications. Later on, Y. Wang *et al.* proposed an A-T-A rasorber with varactor diodes as the active components to tune the transmission frequency [31]. To reduce the insertion loss caused by the series resistance of varactor, a unit cell structure with small capacitance in the resonant tanks of both resistive and FSS layers were used, resulting in the wide transition regions that significantly narrows the absorption bandwidth ($\leq$ 63%). In addition, the device covers a narrow transmission frequency range that limits its implementation in broadband applications. Recently, S. C. Bakshi et.al experimentally demonstrated a reconfigurable rasorber whose passband can be switched among three discrete frequency ranges [32]. Hence, the device is able to operate among A-T, A-T-A and T-A modes. Although this rasorber exhibits over 80% fractional absorption bandwidth in A-T and T-A modes, the passband of the device cannot be tuned continuously, limiting its overall transmission frequency range.

Hence, in this work, a reconfigurable rasorber aiming at extending the overall transmission frequency range is proposed. It combines an electronically controlled resistive layer utilizing the equivalent tunable inductance and mechanically tuned FSS proposed in [33]. Due to the absence of varactors, the FSS exhibits ultra-low insertion loss and can be potentially used for high-performance tunable rasorber design. Although the low-frequency performance of the mechanically tuned FSS has been demonstrated experimentally in [33], the theoretical analysis of its operation principle and the corresponding equivalent circuit model are absent. In addition, its transmission and reflection characteristics at higher frequencies that are favorable for multi-passband rasorber design are not analyzed in detail either. Therefore, in section II of this paper, a detailed investigation of the mechanically tuned FSS, with both frequency and time-domain simulations, over a wide frequency range is presented. In addition, a resistive layer with a reconfigurable resonance tank and compact unit-cell geometry for multi-passband rasorber design is also introduced in section III. Section IV illustrates the equivalent circuit analysis as well as the numerical simulation results of the proposed rasorber. The validation of the proposed reconfigurable rasorber is confirmed with experiment results in Section V. Section VI concludes the paper.

II. TUNABLE FREQUENCY SELECTIVE SURFACE ANALYSIS

The unit-cell structure of the mechanical reconfigurable FSS is presented in Fig. 1(a) and (b). It consists of a rectangular metallic frame with periodicity a and a metallic patch with thick d_p. The thickness of the metallic wall is d' and the gap between the metallic walls is $s = a - d'$. d'' is the length of the metallic wall along the direction of wave prorogation. w_p is the edge length of the square patch. Cylindrical shafts are inserted into the holes of metallic frame to connect the adjacent patches. The square shaft heads prevent the patches

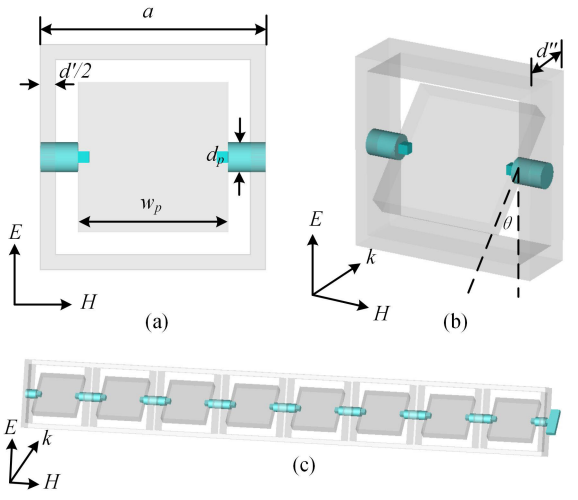

FIGURE 1. Schematic of FSS: (a) front view; (b) side view; (c) 8 × 1 unit cells.

from skidding during the tuning procedure, which guarantees the normal vectors of patches in each row of FSS in parallel with each other at any time. Hence, one can easily tune the angle θ of each row from $-90°$ to $+90°$ by adjusting the knobs attached on the side of FSS, as shown in Fig. 1(c).

A. EQUIVALENT CIRCUIT MODEL OF MECHANICALLY TUNABLE FSS

To investigate the operation principle of this mechanically reconfigurable FSS, an equivalent circuit model (ECM) is derived in this section. The metallic frame can be divided into finite thick metallic gratings in parallel with the direction of the electric field and finite thick metallic gratings in parallel with the direction of the magnetic field, as shown in Fig. 2(a) and (c) respectively. Under normal incident y-polarized wave, the equivalent circuit model of the former gratings can be presented as Fig. 2(b), in which B_a and B_b are calculated as [34]

$$B_a = B_1 + \frac{aY_0}{s}\tan\frac{\pi d''}{\lambda}, \tag{1}$$

$$B_b = \frac{aY_0}{s}\csc\frac{2\pi d''}{\lambda}, \tag{2}$$

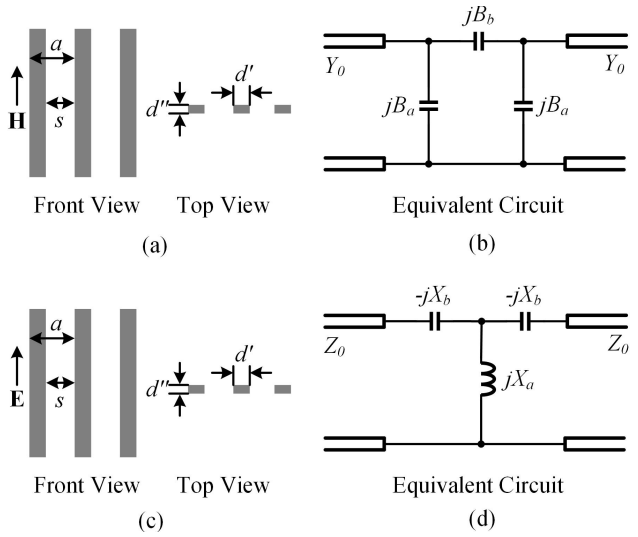

FIGURE 2. Infinitely extended metallic gratings with finite thickness and axes parallel with (a) the magnetic of normal incidence and (b) the corresponding equivalent circuit. Infinitely extended metallic gratings with finite thickness and axes parallel with (c) the electric field of normal incidence and (d) the corresponding equivalent circuit.

where $Y_0 = 1/Z_0$, Z_0 is impedance of free space, λ is the wavelength at frequency of interest,

$$B_1 = \frac{2aY_0}{\lambda}\left[\ln\sec\left(\frac{\pi}{2}\frac{d'}{a}g\right) - \frac{\pi}{2}\frac{d'd''}{as} + \frac{A\sin^4\frac{\pi d'}{2a}}{1+A\cos^4\frac{\pi d'}{2a}} + \frac{1}{16}\left(\frac{a}{\lambda}\right)^2\left(1-3\cos^2\frac{\pi d'}{2a}\right)^2\sin^4\frac{\pi d'}{2a}\right], \tag{3}$$

$$g \approx 1 + \frac{d''}{\pi d'}\ln\left(\frac{4\pi}{e}\cdot\frac{d'}{d''}\right), \tag{4}$$

and

$$A = \frac{1}{\sqrt{1-\left(\frac{a}{\lambda}\right)^2}} - 1. \tag{5}$$

Consequently, the equivalent circuit model of the later gratings can be presented as Fig. 2(d), in which X_a and X_b are calculated as [34]

$$X_a = \frac{aZ_0}{\lambda}\left\{\ln\frac{a}{2\pi r_0} + \frac{1}{2}\sum_{\substack{m=-\infty\\ m\neq 0}}^{\infty}\left[\frac{1}{\sqrt{m^2-\left(\frac{a}{\lambda}\right)^2}} - \frac{1}{|m|}\right]\right\}, \tag{6}$$

$$X_b = \frac{aZ_0}{\lambda}\left(\frac{2\pi r_1}{a}\right)^2, \tag{7}$$

where

$$r_0 \approx \frac{d'}{4}\left[1 + \frac{d''}{\pi d'}\ln\left(4\pi e\frac{d'}{d''}\right)\right], \tag{8}$$

$$r_1 \approx \frac{d''}{2\sqrt{2}}\left[1 + \frac{d'}{\pi d'}\ln\left(\frac{4\pi}{e}\frac{d''}{d'}\right)\right], \tag{9}$$

and $e \approx 2.718$ is the base of the natural logarithm.

When the metallic patch is placed in the center of the unit cell, additional capacitances are induced between the patch and walls. To calculate the capacitance between two vertically placed metallic plates with finite thickness, as shown in Fig. 3, the overall capacitance C_t is divided into C_L, C_M and C_R, in which C_L and C_R can be calculated as [35]

$$C_{L/R} = C_{L/R\_in} + C_{L/R\_out}, \tag{10}$$

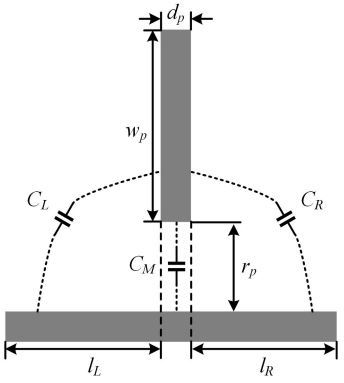

FIGURE 3. Vertically placed metallic plates with finite thickness.

where

$$C_{L/R\_in} = \epsilon_0\frac{K'\left(k_{L/R\_in}\right)}{K\left(k_{L/R\_in}\right)}, \tag{11}$$

$$C_{L/R\_out} = \epsilon_0\frac{K'\left(k_{L/R\_out}\right)}{K\left(k_{L/R\_out}\right)}, \tag{12}$$

$$k_{L/R\_in} = \frac{r_p}{r_p+w_p}\sqrt{\frac{\left(r_p+w_p\right)^2+l_{L/R}^2}{r_p^2+l_{L/R}^2}}, \tag{13}$$

$$k_{L/R\_out} = \sqrt{\frac{r_p^{(2/3)}\left(\left(r_p + w_p\right)^{(2/3)} + l_{L/R}^{(2/3)}\right)}{\left(r_p + w_p\right)^{(2/3)}\left(r_p^{(2/3)} + l_{L/R}^{(2/3)}\right)}}, \quad (14)$$

$$K'(k) = K(k'), \quad (15)$$

$K(k)$ is the complete elliptic of the first kind and k' is the complementary modulus of k. Consequently, the middle capacitance can be estimated with the classical equation used for a parallel plate capacitor as

$$C_M = \frac{\epsilon_0 w_p d_p}{r_p}, \quad (16)$$

and the overall capacitance C_{tot} is

$$C_{tot} = C_R + C_M + C_L. \quad (17)$$

Hence, the corresponding capacitance in ECM is $C_t = C_{tot}/2$ due to the series connection of two identical C_{tot} and the final equivalent circuit model of the metallic walls can be illustrated as Fig. 4 (a), in which $C_{ag} = B_a/\omega$,$C_{bg} = B_b/\omega$, $L_{al} = X_a/\omega$, $C_{bl} = 1/\omega X_b$. To derive an analytical expression for the S parameters of proposed FSS, a conversion from T- to π-network is required, resulting in the ECM shown in Fig. 4 (b), where

$$Z_{bf} = \frac{j - j(C_t + 2C_{bl})L_{al}\omega^2}{-C_{bg}\omega + (C_t C_{bg} + 2C_{bl}C_{bg} + C_{bl}^2)L_{al}\omega^3}, \quad (18)$$

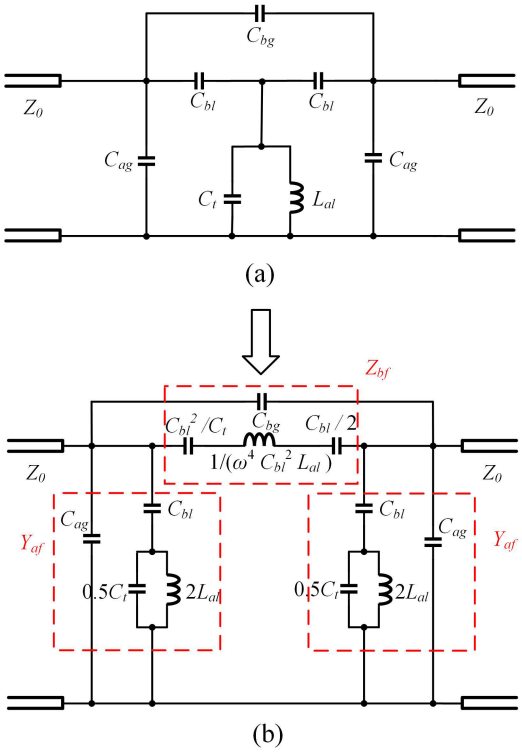

FIGURE 4. (a) ECM of mechanically tunable FSS; (b) ECM after T-to-π network transformation.

and

$$Y_{af} = j\omega(C_{ag} + \frac{C_{bl}(C_t L_{al}\omega^2 - 1)}{(C_t + 2C_{bl})L_{al}\omega^2 - 1}) \quad (19)$$

are the impedance and admittance of the π-network. Hence, the ABCD matrix of proposed FSS is presented as

$$\begin{bmatrix} A & B \\ C & D \end{bmatrix} = \begin{bmatrix} 1 & 0 \\ Y_{af} & 1 \end{bmatrix}\begin{bmatrix} 1 & Z_{bf} \\ 0 & 1 \end{bmatrix}\begin{bmatrix} 1 & 0 \\ Y_{af} & 1 \end{bmatrix} = \begin{bmatrix} Z_{bf}Y_{af} + 1 & Z_{bf} \\ 3Y_{af} + Z_{bf}Y_{af}^2 & Z_{bf}Y_{af} + 1 \end{bmatrix}, \quad (20)$$

and the $|S_{21}|$ of proposed FSS can be derived as

$$|S_{21}|_{FSS} = \left|\frac{2}{A + B/Z_0 + CZ_0 + D}\right|. \quad (21)$$

At frequency

$$f = \frac{\sqrt{C_{ag} + C_{bl}}}{\sqrt{2C_{ag}C_{bl}L_{al} + C_{ag}C_t L_{al} + C_{bl}C_t L_{al}}}, \quad (22)$$

one have $Y_{af} = 0$ and

(21) can be simplified as

$$|S_{21}|_{FSS} = \left|\frac{2Z_0}{2Z_0 + Z_{bf}}\right|. \quad (23)$$

Therefore, EM waves can propagate through the device with a low insertion loss if $|Z_{bf}| \ll Z_0$. In addition, With the help of the angle marks printed on the side of each row, the rotation angle θ can be controlled accurately. Therefore, C_t can be varied and transmission frequency is tuned correspondingly.

B. ECM, SIMULATION AND MEASUREMENT RESULTS OF FSS

Fig. 5(a) and (b) demonstrate the numerical simulation results and the theoretical results calculated with ECM from 1.5 to 12 GHz. As the frequency-domain solver of CST microwave studio provides excellent simulation accuracy for devices consisting of identical periodic unit cells, the corresponding simulation results achieved for frequency between 1.5 to 8 GHz are presented in the white area of Fig. 5(a) and (b). When $f = 8 \sim 12$ GHz, the results achieved from the frequency-domain solver exhibit a lot of unexpected spikes that cannot be used to predict the device performance at all. Hence, the time-domain solver is used instead to achieve the required simulation results, as shown in the light blue area of Fig. 5(a) and (b). Although it does not provide accurate resonant frequency prediction compared with the frequency-domain counterpart, it is still a good tool for investigating the performance of a device when the results achieved from frequency-domain solver are not valid. It is worth mentioning that in the rest of the paper, the white areas illustrate the simulation results achieved from frequency-domain solver while the light blue area depicts the results achieved from time-domain solver for figures demonstrating numerical simulation results as well.

The geometrical parameters used in the simulations are as follows: $a = 30$ mm, $w_p = 20$ mm, $d_p = 4$ mm, $d' = 4$ mm,

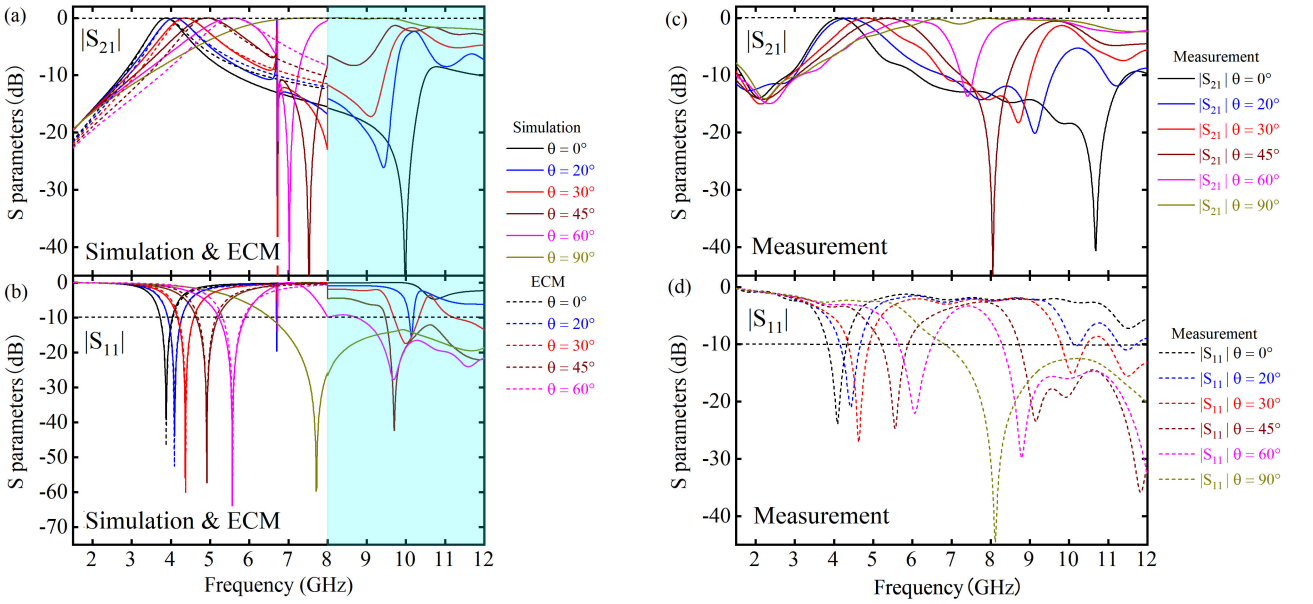

FIGURE 5. S parameters of the proposed FSS: (a) $|S_{21}|$ of numerical simulation and ECM calculation; (b) $|S_{11}|$ of numerical simulation and ECM calculation; (c) Measured $|S_{21}|$; (d) Measured $|S_{11}|$. The white area in (a) and (b) illustrates the simulation results achieved with frequency-domain solver and the light blue area depicts the results achieved with time-domain solver.

$d'' = 10$ mm. The capacitance of $\theta = 0°$ is achieved with (17) and those of non-zero angles, as shown in Fig. 6, are extracted by fitting the theoretical calculation to the numerical simulation results. It can be seen that results calculated with the proposed ECM agree excellently with the numerical simulation results below 5 GHz and a tunable passband with a center frequency between 3.9 to 5.6 GHz is observed. When the frequency increases so that a exceeds $\lambda/2$, the deviations between ECM and simulation results increase as the equations of ECM are valid for $a \leq \lambda/2$ only [34]. For frequency above 8 GHz, the simulation results achieved with time-domain solver predicts an extra tunable transmission band centered around 9∼10 GHz.

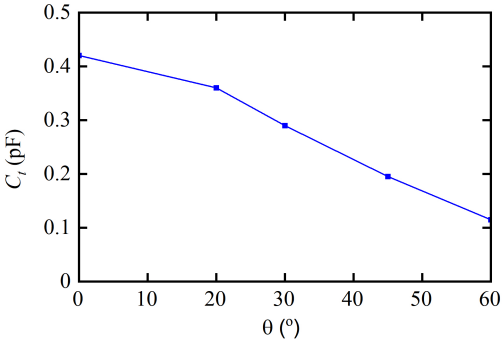

FIGURE 6. C_t vs. θ extracted from numerical simulations.

To validate the results achieved from theoretical analysis, the FSS is fabricated with aluminum as shown in Fig. 7, in which the marks help to accurately control the rotation angle of FSS are also illustrated. Fig. 5(c) and (d) demonstrate

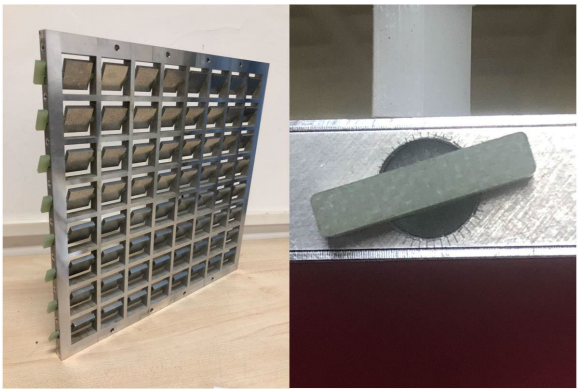

FIGURE 7. Photograph of the fabricated FSS and control knob with angle marks.

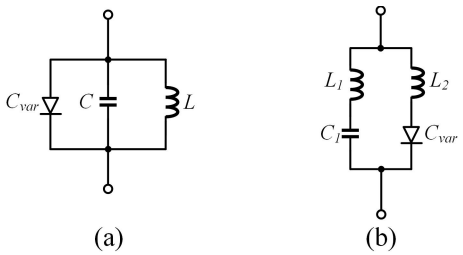

FIGURE 8. (a) The resonant tank of resistive layer in [30] and [31]. (b) Resonant tank used in this work.

the corresponding S parameters achieved with free space measurement. The device exhibits a tunable passband centered from 4.13 to 6.61 GHz when θ varies from 0° to 90°. The simulation results are well reproduced with laboratory measurements except at frequencies above 8 GHz due to the

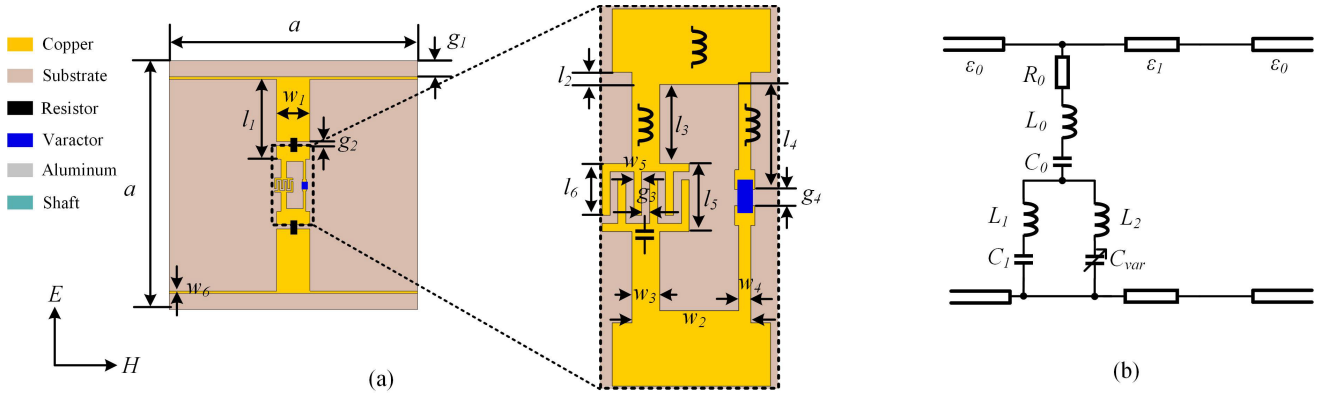

FIGURE 9. (a) Physical geometry of the proposed resistive layer; (b) ECM of the proposed resistive layer.

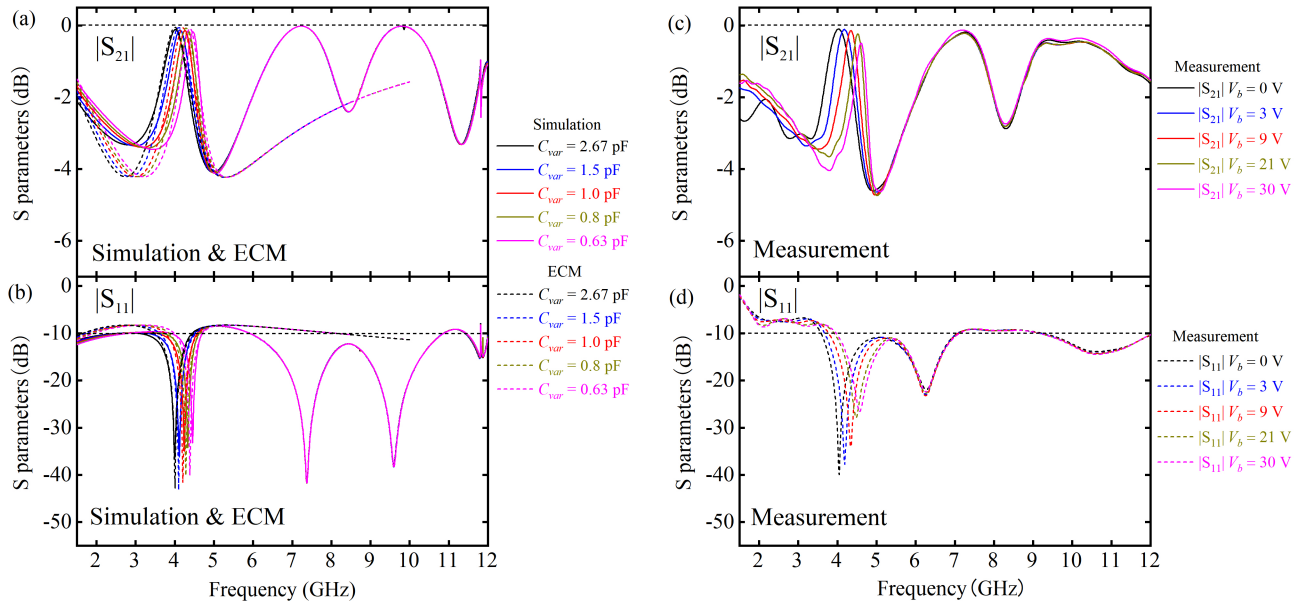

FIGURE 10. S parameters of the proposed resistive layer:(a) $|S_{21}|$ of numerical simulation and ECM calculation; (b) $|S_{11}|$ of numerical simulation and ECM calculation; (c) Measured $|S_{21}|$; (d) Measured $|S_{11}|$. The circuit components in ECM are $R_0 = 300\ \Omega$, $L_0 = 8$ nH, $C_0 = 0.248$ pF, $L_1 = 2.89$ nH, $C_1 = 0.18$ pF, $L_2 = 6.12$ nH.

poor simulation accuracy of time-domain solver. However, the second tunable passband at higher frequencies for $45° \leq \theta \leq 90°$, as predicted by the numerical simulation, is also observed in the measurement results. Therefore, the proposed FSS is potentially suitable for the design of rasorbers with dual or multiple reconfigurable passbands.

III. TUNABLE RESISTIVE LAYER ANALYSIS

The frequency reconfiguration of the resistive layer is realized with varactor diodes. As well known, the capacitance of varactor diode can be tuned by varying the reverse bias voltage applied between its anode and cathode. In [30] and [31], the varactor diodes are connected in parallel with the geometrical capacitance, as shown in Fig. 8(a), resulting in a tunable capacitance to control the resonance frequency. The disadvantage of this design is that the bias voltage cannot be directly applied on the varactor as a DC short circuit is caused by the inductor, resulting in a complicated bias network distributed on multiple metallic layers of the device [30], [31].

A. RECONFIGURABLE RESISTIVE LAYER

In this work, the reconfigurable resistive layer is designed utilizing a resonant tank with two parallel-connected series LC, as shown in Fig. 8(b). L_2, L_1 and C_1 are the geometrical inductors and capacitor, respectively. As $j\omega L_2$ is much greater than $j/\omega C_{var\_max}$ within the frequency of interest, the overall reactance of series L_2-C_{var} is inductive. Hence, by varying the reverse bias voltage, a tunable inductance is realized. Since the capacitance of varactor diode is maximized at $V_b = 0$, the resultant tunable inductance branch exhibits its maximum inductance and hence introduces a relatively low insertion

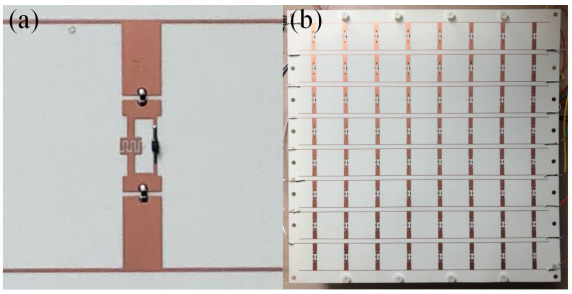

FIGURE 11. Photograph of the fabricated resistive layer: (a) a single unit-cell; (b) the whole device.

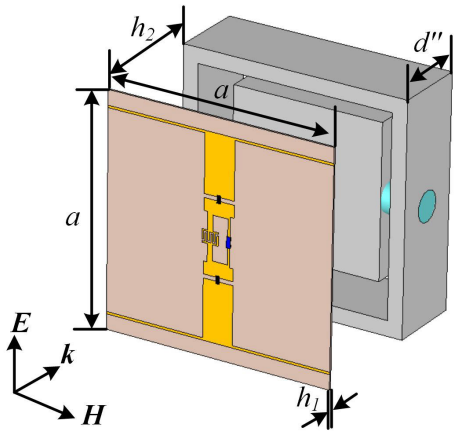

FIGURE 12. Unit cell of the proposed rasorber.

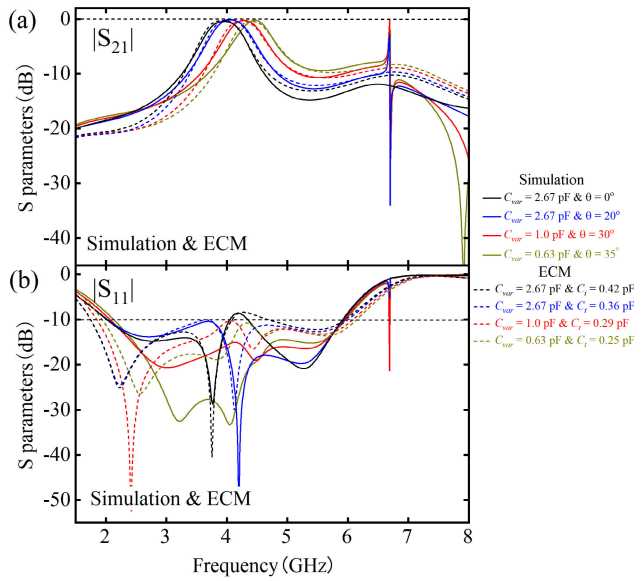

FIGURE 13. ECM and numerical simulation results of the proposed rasorber.

loss to the resultant rasorber. In addition, unlike the equivalent circuit illustrated in Fig. 8(a), the proposed approach allows the implementation of bias voltage directly on the ports of the varactors in Fig. 8(b). Hence, the bias network is embedded in the unit-cell configurations which greatly simplifies the design process.

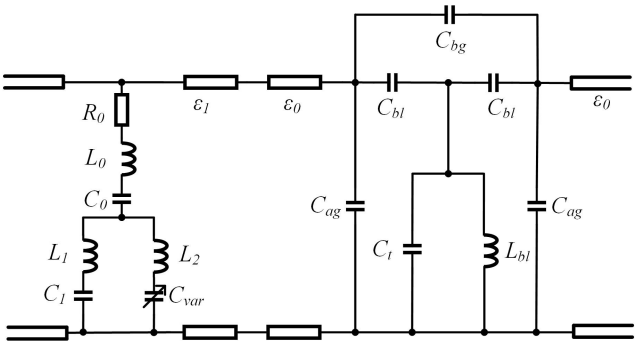

FIGURE 14. ECM of the proposed rasorber.

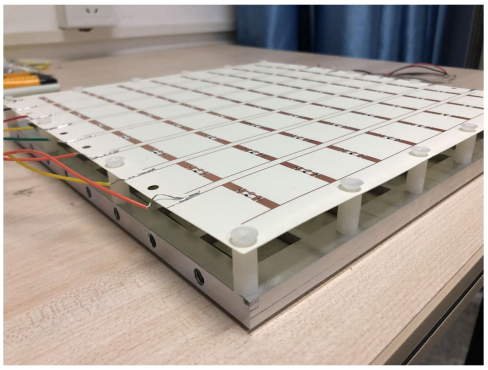

FIGURE 15. Photograph of the fabricated rasorber.

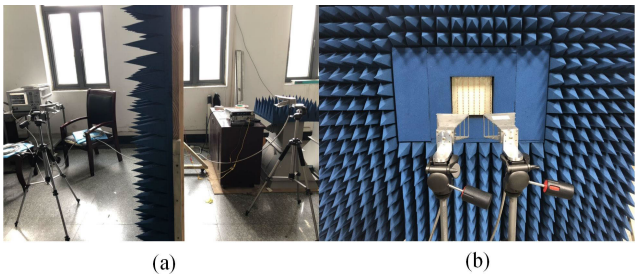

FIGURE 16. Free space measurement setup of the proposed rasorber: (a) transmission; (b) reflection.

Fig. 9(a) and (b) illustrate the schematic and equivalent circuit model of a resistive layer designed utilizing the proposed resonant tank with reconfigurable inductance. The series R_0-L_0-C_0 is used to match the impedance of free space for wave absorption and the transmission band is generated with the resonant tank presented in Fig. 8(b).

Obviously, by varying the external bias voltage, C_{var} is tuned and the transmission frequency of the resistive layer is varied as well.

B. ECM, SIMULATION AND MEASUREMENT OF RESISTIVE LAYER

Fig. 10(a) and (b) present the results achieved with numerical simulation and ECM calculation results of the resistive layer. To match the passband of FSS presented in the last section,

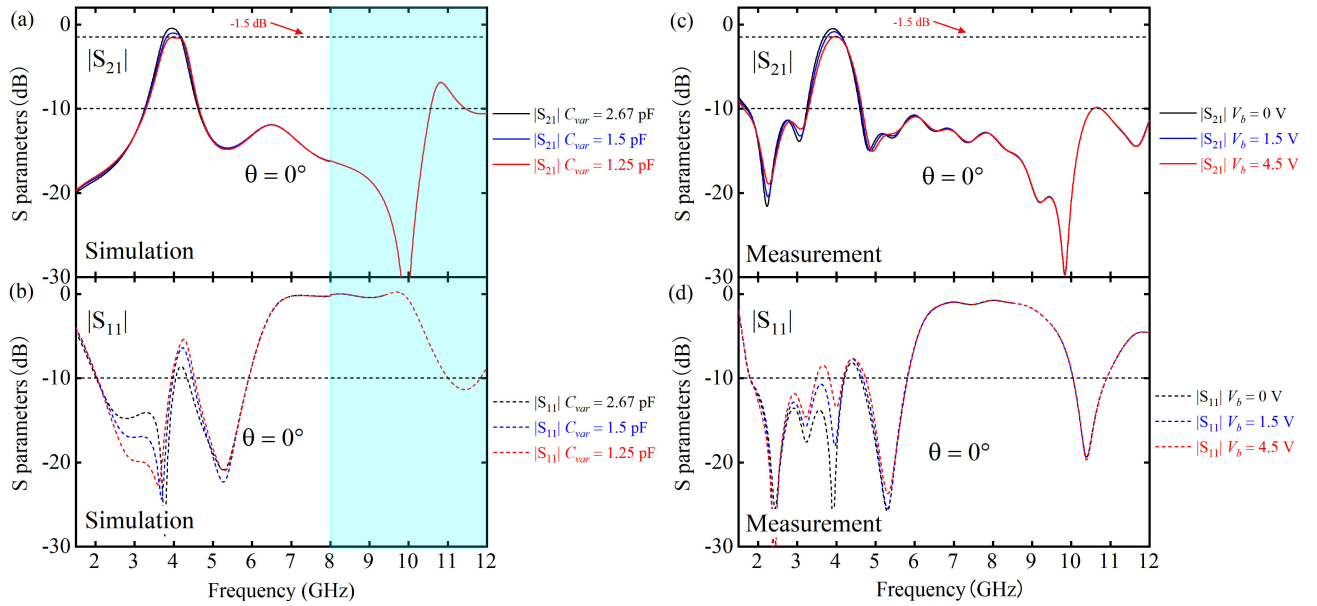

FIGURE 17. S parameters of the proposed rasorber under $\theta = 0°$ and various V_b: (a) and (b) illustrate the simulation results; (c) and (d) illustrate the measurement results. The white area of (a) and (b) illustrate the simulation results achieved with frequency-domain solver and the light blue area depicts the results achieved with time-domain solver.

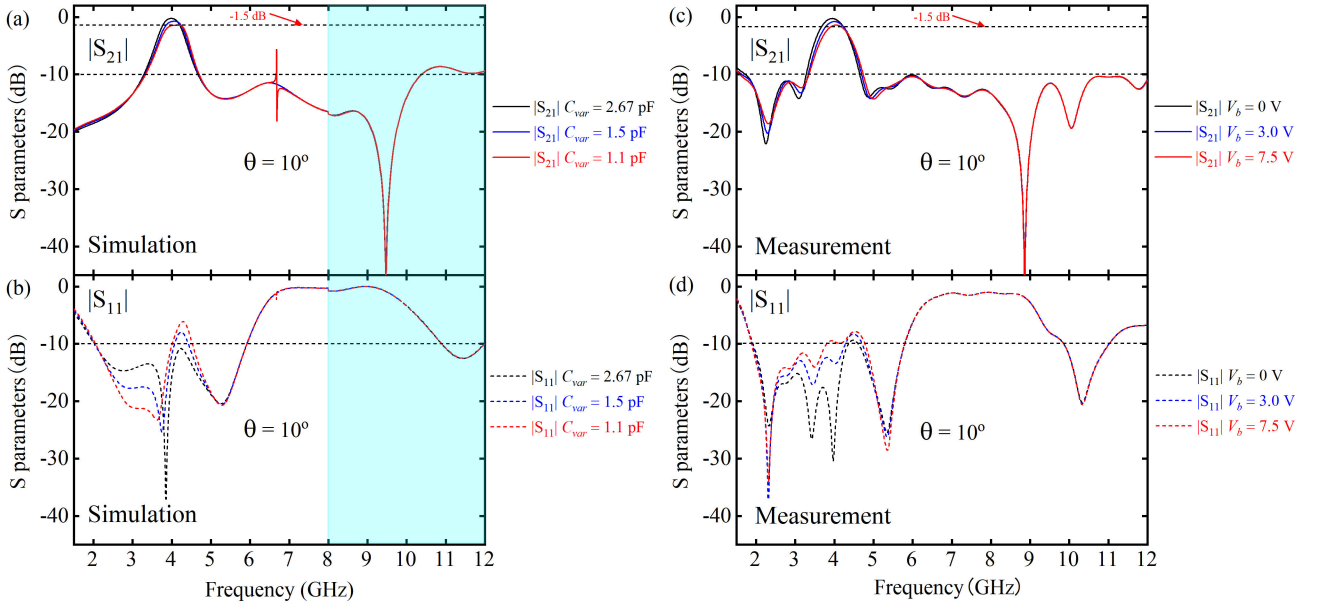

FIGURE 18. S parameters of the proposed rasorber under $\theta = 10°$ and various V_b: (a) and (b) illustrate the simulation results; (c) and (d) illustrate the measurement results. The white area of (a) and (b) illustrate the simulation results achieved with frequency-domain solver and the light blue area depicts the results achieved with time-domain solver.

the following geometry parameters are used: $h_1 = 0.254$ mm, $w_1 = 4$ mm, $w_2 = 3$ mm, $w_3 = 0.7$ mm, $w_4 = 0.3$ mm, $w_5 = 0.2$ mm, $w_6 = 0.3$ mm, $l_1 = 9.6$ mm, $l_2 = 0.3$ mm, $l_3 = 2$ mm, $l_4 = 2.65$ mm, $l_5 = 1.7$ mm, $l_6 = 1.3$ mm, $g_1 = 1.95$ mm, $g_2 = 0.5$ mm, $g_3 = 0.2$ mm, $g_4 = 0.4$ mm. The substrate is Rogers 4350B with relative permittivity $\epsilon_r = 3.48$ and loss tangent $\tan\delta = 0.0037$. Since there is a parasitic resistance R_s in series with the varactor that can cause significant insertion loss to the passband, the varactor diode SMV1405 manufactured by Skyworks with a low R_s of 0.8 Ω and parasitic inductance of 0.45 nH was selected for this work. The capacitance of varactor can be tuned between approximately 2.7∼0.6 pF when V_b varies within 0∼30 V.

Again, the ECM results agree well with the numerical simulation at frequency below 5 GHz only due to the increase of ratio a/λ (exceeding 1/2) when the frequency increases.

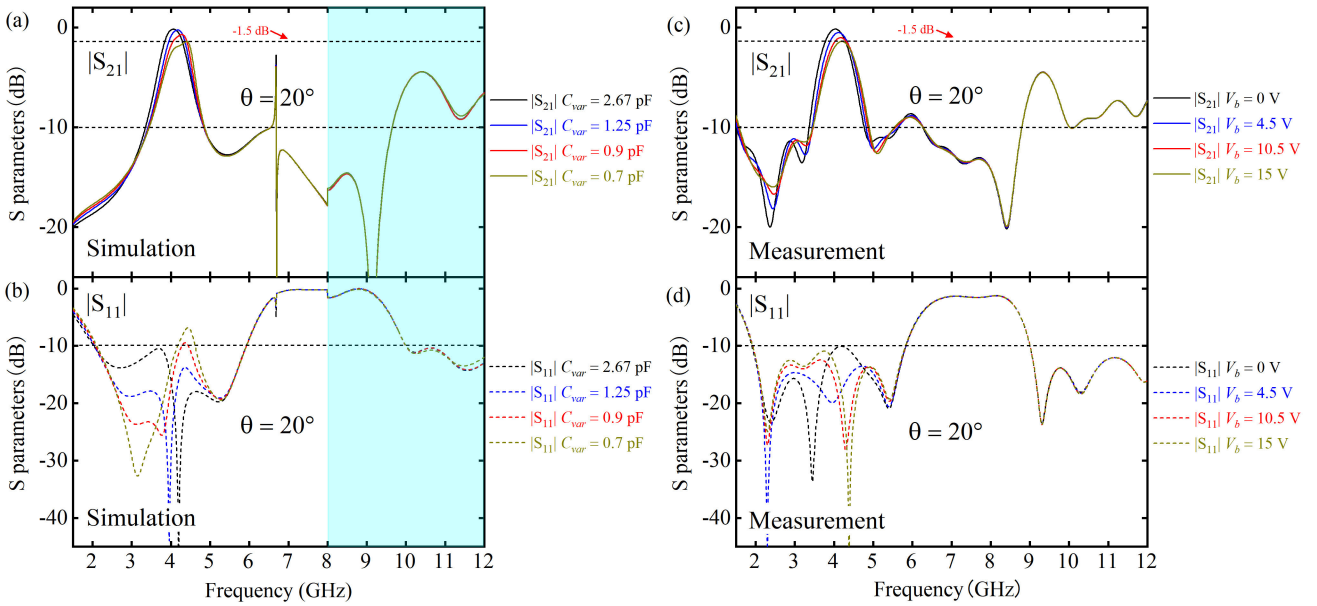

FIGURE 19. S parameters of the proposed rasorber under $\theta = 20°$ and various V_b: (a) and (b) illustrate the simulation results; (c) and (d) illustrate the measurement results. The white area of (a) and (b) illustrate the simulation results achieved with frequency-domain solver and the light blue area depicts the results achieved with time-domain solver.

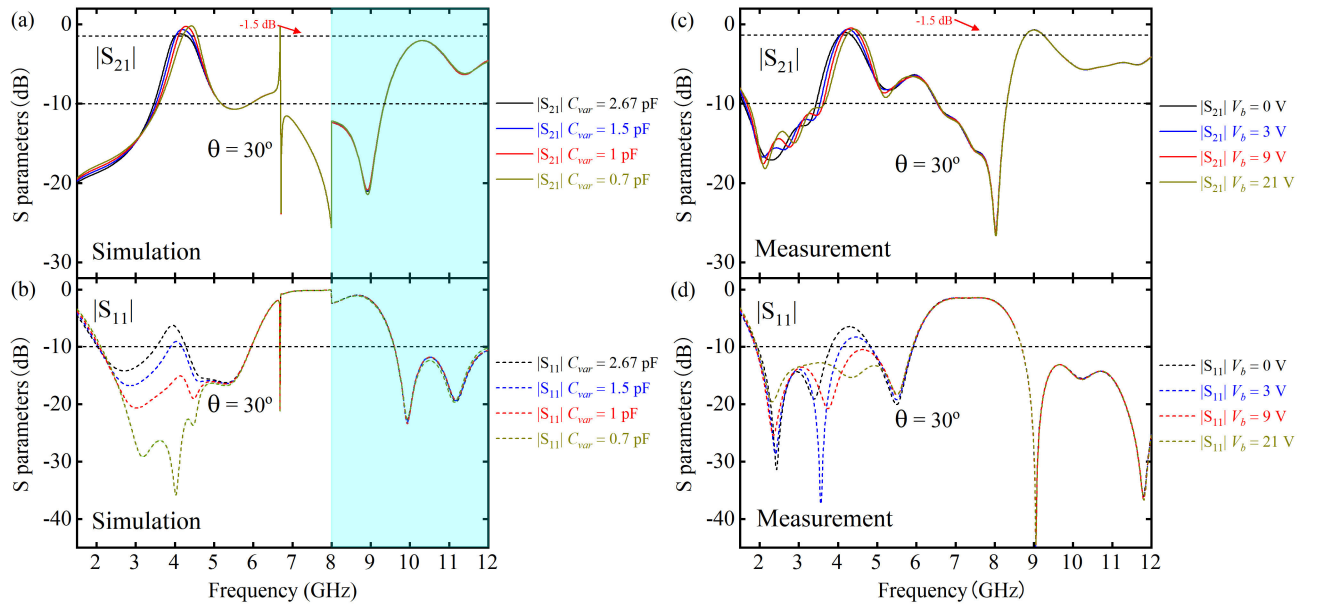

FIGURE 20. S parameters of the proposed rasorber under $\theta = 30°$ and various V_b: (a) and (b) illustrate the simulation results; (c) and (d) illustrate the measurement results. The white area of (a) and (b) illustrate the simulation results achieved with frequency-domain solver and the light blue area depicts the results achieved with time-domain solver.

Fig. 11 illustrates the photograph of the fabricated resistive layer. The corresponding measurement results are presented in Fig. 10(c) and (d). It can be seen that the measurement and simulation results agree well with each other over the whole frequency of interest and a continuously tunable passband centered from 4.03 to 4.61 GHz is observed, matching excellently with the lower passband of FSS. At higher frequencies, the resistive layer is nearly transparent to EM waves except for a narrow frequency range of 7.90∼8.76 GHz, making it suitable for rasorber design with multiple passbands as well.

IV. ECM VS. SIMULATION RESULTS OF RASORBER

The reconfigurable rasorber proposed in this work is designed utilizing the FSS and resistive layer presented above, whose unit-cell configuration is presented in Fig. 12 with an air spacer thickness of $h_2 = 16$ mm. The operation principle

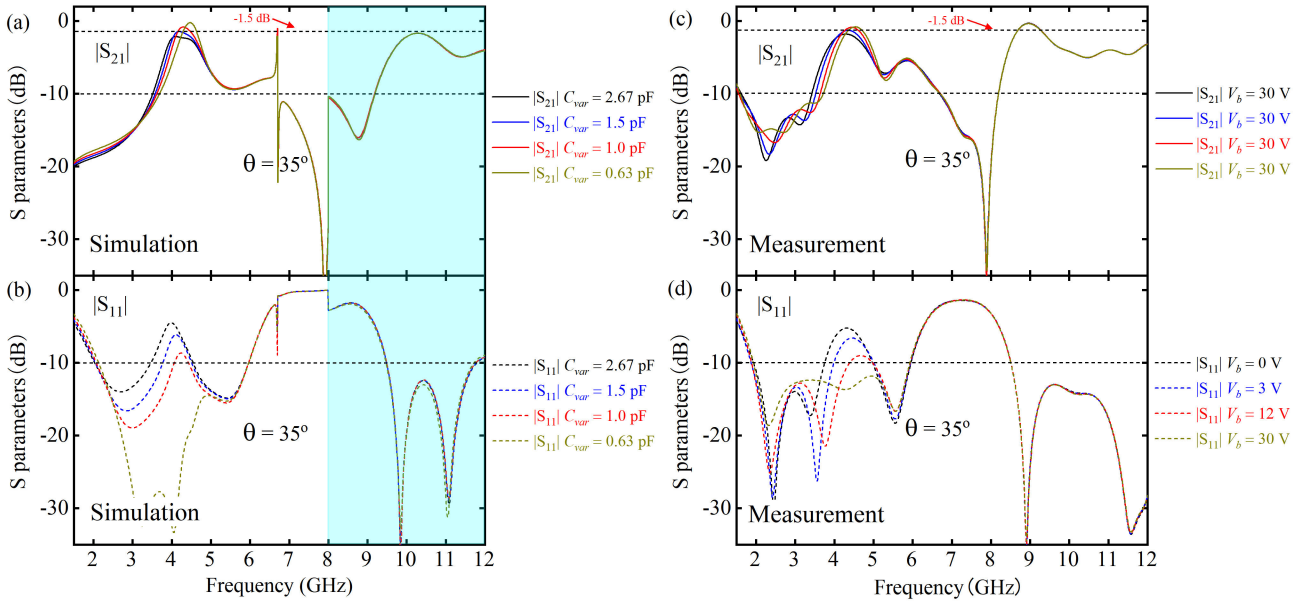

FIGURE 21. S parameters of the proposed rasorber under $\theta = 35°$ and various V_b: (a) and (b) illustrate the simulation results; (c) and (d) illustrate the measurement results. The white area of (a) and (b) illustrate the simulation results achieved with frequency-domain solver and the light blue area depicts the results achieved with time-domain solver.

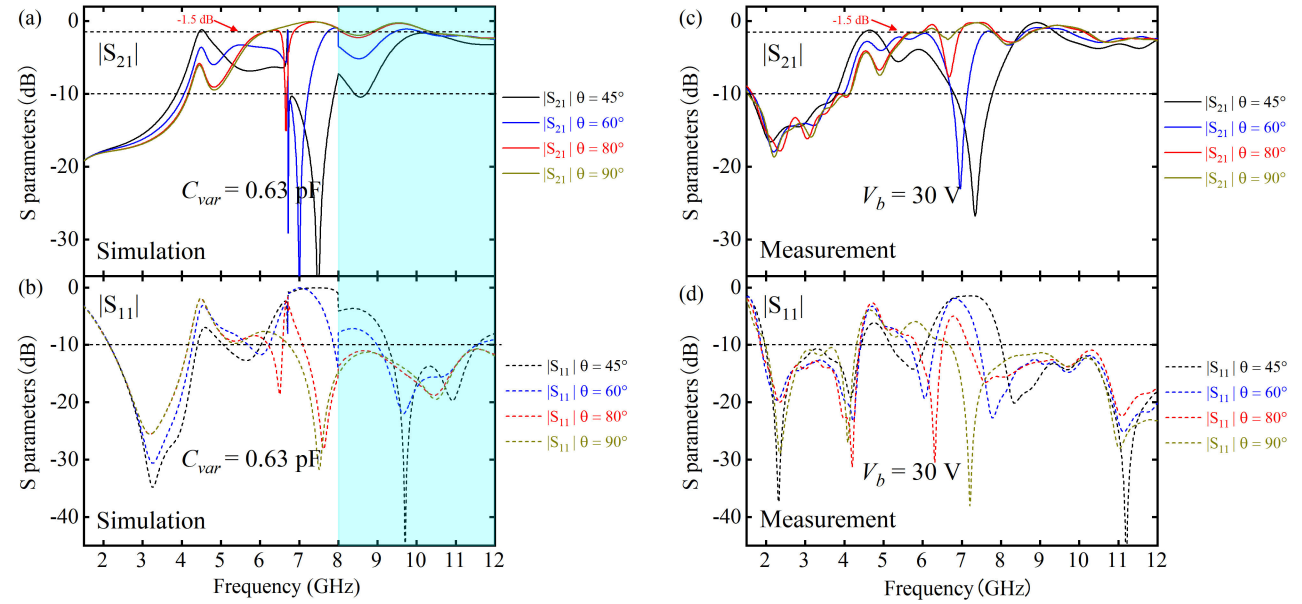

FIGURE 22. S parameters of the proposed rasorber under $\theta = 45° \sim 90°$ and $V_b = 30$ V: (a) and (b) illustrate the simulation results; (c) and (d) illustrate the measurement results. The white area of (a) and (b) illustrate the simulation results achieved with frequency-domain solver and the light blue area depicts the results achieved with time-domain solver.

of rasorbers have been introduced in details in [1]–[25]. The basic idea behind a reconfigurable rasorber is to tune the passbands of FSS and resistive layer simultaneously, so that their transmission bands are always matched and a tunable transmission window can be created for the rasorber. As introduced above, it is obvious that the lower-frequency transmission window of the proposed rasorber should be tuned by rotating the metallic patch in FSS (i.e. C_t) and adjusting the reverse bias voltage of varactor diode (i.e. C_{var}) simultaneously. At higher frequencies, as the resistive layer exhibits two wide bias-independent passbands, the passband(s) of rasorber is(are) controlled by just mechanically tuning the rotation angle (i.e. θ) of FSS.

Since the FSS exhibits a small resonant frequency variation between $\theta = 0°$ to $10°$, the simulation results of proposed rasorber under $\theta = 0°, 20°, 30°$ and $35°$ are presented

TABLE 1. Measurement result conclusions.

θ	$V_{b(\mathrm{IL_{min}})}$	$\mathrm{IL_{min}}$	$f_{(\mathrm{IL_{min}})}$	Absorption Band(s) (i.e.$\lvert S_{11}\rvert \leq -10$ & dB $\lvert S_{21}\rvert \leq -10$ dB)	Transmission Band(s) (i.e. $\lvert S_{21}\rvert \geq -1.5$ dB)
0°	0 V	0.5 dB	3.91 GHz	1.8∼3.25 GHz (57.4%) 4.63∼5.80 GHz (22.4%) 10.05∼10.9 GHz (8.1%)	3.68∼4.15 GHz (12.0%)
10°	0 V	0.26 dB	3.95 GHz	1.93∼3.27 GHz (51.5%) 4.65∼5.80 GHz (22.0%) 9.86∼11.01 GHz (11.0%)	3.69∼4.21 GHz (13.1%)
20°	0 V	0.16 dB	4.03 GHz	1.91∼3.36 GHz (62.6%) 4.77∼5.64 GHz (16.7%)	3.77∼4.3 GHz (13.1%)
30°	9 V	0.45 dB	4.33 GHz	1.9∼3.65 GHz (63.1%)	4.2∼4.63 GHz (9.7%)
35°	30 V	0.8 dB	4.54 GHz	1.94∼3.71 GHz (62.7%)	4.32∼4.74 GHz (9.3%)
45°	30 V	0.21 dB	8.92 GHz	1.97∼3.78 GHz (63.0%)	4.51∼4.77 GHz (5.6%) 8.52∼9.39 GHz (9.7%)
60°	30 V	0.90 dB	8.91 GHz	1.87∼3.95 GHz (71.5%)	7.55∼7.95 GHz (5.2%) 8.62∼9.74 GHz (12.2%)
80°	30 V	0.20 dB	7.51 GHz	1.87∼4.12 GHz (75.1%)	5.99∼6.4 GHz (6.6%) 6.97∼7.84 GHz (11.8%) 8.75∼10.13 GHz (14.6%)
90°	30 V	0.22 dB	7.39 GHz	1.99∼4.11 GHz (69.5%)	6.03∼6.39 GHz (5.8%) 6.85∼7.79 GHz (12.8%) 8.79∼10.2 GHz (13.1%)

as solid lines in Fig. 13. It can be seen that when both θ and C_{var} are tuned, the device demonstrates a low $\mathrm{IL_{min}}$ between 0.11 to 0.49 dB while the $\mathrm{IL_{min}}$ frequency varies from 3.94 to 4.52 GHz. Hence, the frequency range covered for $|S_{21}| \geq -1.5$ dB at lower frequency is between 3.74 to 4.69 GHz, covering a fractional transmission bandwidth of 22.5%. In addition, the device also exhibits low microwave reflection (i.e. $|S_{11}| < -10$ dB) between approximately 2 to 6 GHz for all angles except $\theta = 0°$. Moreover, the ECM of the proposed raosrber is shown in Fig. 14 and the corresponding mathematical modelling results are also plotted as dashed lines in Fig. 13, demonstrating excellent agreement with the numerical simulation at frequency below 5 GHz. The detailed performance of proposed rasorber over 1.5∼12 GHz is investigated with numerical simulations and laboratory experiments in the following section.

V. MEASUREMENT AND SIMULATION RESULTS OF RASORBER

Fig. 15 demonstrates the photograph of proposed rasorber consisting of 8 × 8 unit cells with an overall dimension of 260 × 260×26 $\mathrm{mm^3}$. The free space measurement, as illustrated in Fig. 16, is carried out to investigate its transmission and reflection characteristics under normal and oblique incident waves as well.

A. NORMAL INCIDENCE

The device performance under normal incident waves is presented in this part. Fig. 17 to 21 illustrate the measured and simulated S parameters of the proposed device when V_b is varied under fixed angles $\theta = 0°, 10°, 20°, 30°, 35°$. As can be seen, the measurement and simulation results agree excellently and the passband can be tuned from a center frequency of 3.91 GHz to 4.54 GHz while the device performance is nearly independent of the voltage variation above

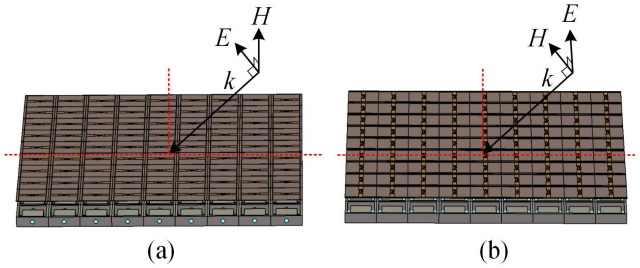

FIGURE 23. Schematic of oblique incidence: (a) TM; (b) TE.

6 GHz under a fixed θ. For $\theta = 0°$ and 10°, except the two absorption bands adjacent to the passband of rasorber, a third absorption band is also observed around the center frequency of 10.5 GHz, as predicted by the time-domain simulation with a frequency shift that caused by the inaccurate resonant frequency prediction of time-domain solver. Further increasing θ to 20°, the highest absorption band disappears and the second absorption band on the right side of passband also narrows. For $\theta = 30°$ and 35°, the second absorption band is also eliminated and the device exhibits a transform from A-T-A to A-T type. When $\theta \geq 35°$, since the high-frequency performance is independent of the external bias voltage and the device exhibits the widest absorption bandwidth under $V_b = 30$ V, the rasorber is characterized with $V_b = 30$ V in the following discussions.

As can be seen in Fig. 22, when θ increases to 45° and 60°, the device exhibits a single absorption band at lower frequencies and two passbands at higher frequencies. Further increasing θ to 80° and 90°, the device exhibit three passbands above the absorption band. The simulation results are well reproduced with measurement results and the performance of the proposed rasorber is summarized in Table 1. The device exhibits a fractional absorption bandwidth between

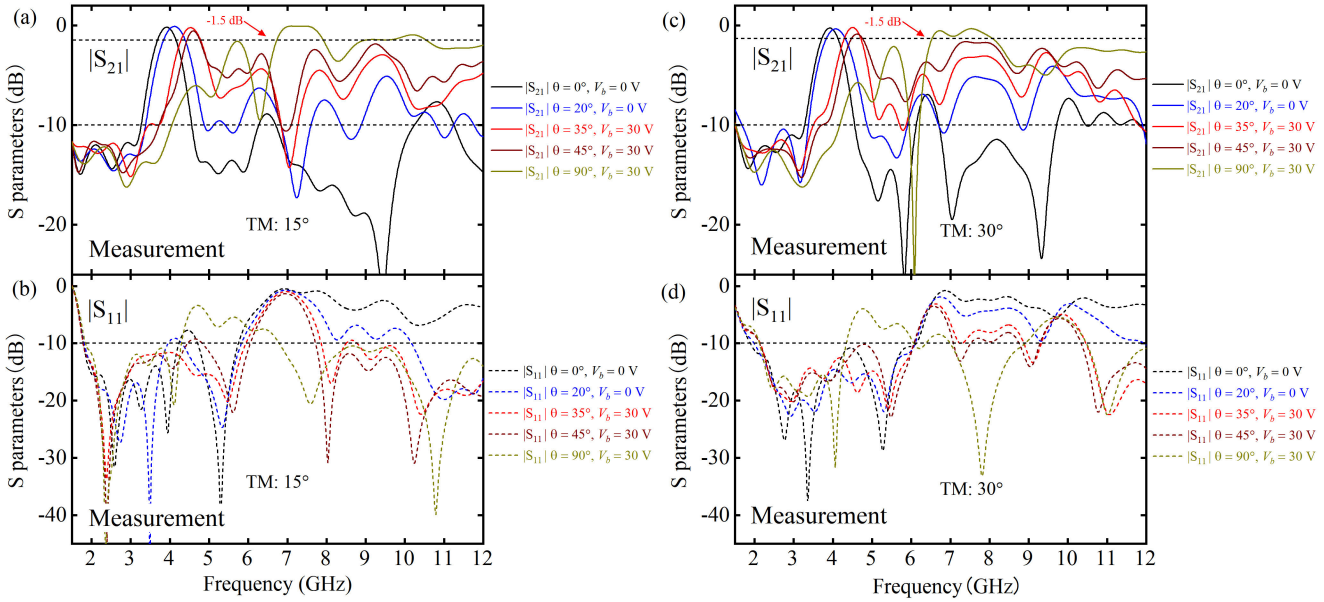

FIGURE 24. Measured S parameters of proposed rasorber under TM oblique incidence. (a) and (b): 15°; (c) and (d): 30°.

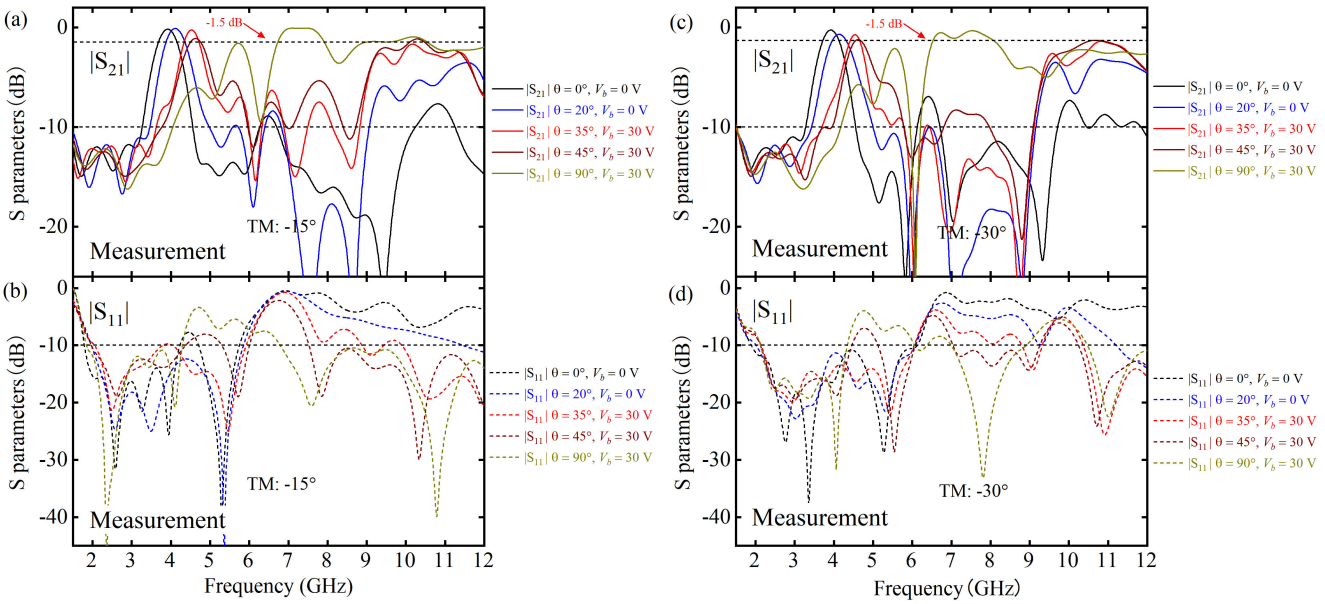

FIGURE 25. Measured S parameters of proposed rasorber under TM oblique incidence. (a) and (b): −15°; (c) and (d): −30°.

62.7% and 88% (57.4%+22.5%+8.1%) and a measured minimum IL_{min} of 0.16 dB is achieved at $\theta = 20°$ and $V_b = 0$ V. The fractional transmission frequency range varies between 9.3% to 23% (6.6%+11.8%+14.6%) and the passband covers 3.68 ∼ 4.77 GHz (25.8%), 5.99 ∼ 6.4 GHz (6.6%), 6.85 ∼ 7.84 GHz (13.5%) and 8.52 ∼ 10.2 GHz (18.0%), corresponding to an overall fractional transmission frequency range of 25.8%+6.6%+13.5%+18.0%=63.9%.

To investigate the novelty of this work, the measurement results of proposed rasorber are compared with the measurement results achieved for other existing scenarios. Table 2 summarizes the comparison of the proposed device with other published reconfigurable rasorbers. The proposed device exhibits a maximum absorption bandwidth of 87.9%, comparable with the state-of-art maximum absorption bandwidth (88.09%) achieved in [28]. While the other reconfigurable rasorbers exhibit a single passband under all conditions, the proposed rasorber can be switched between modes with single, dual and triple transmission bands with at least one absorption band. Hence, the proposed device greatly

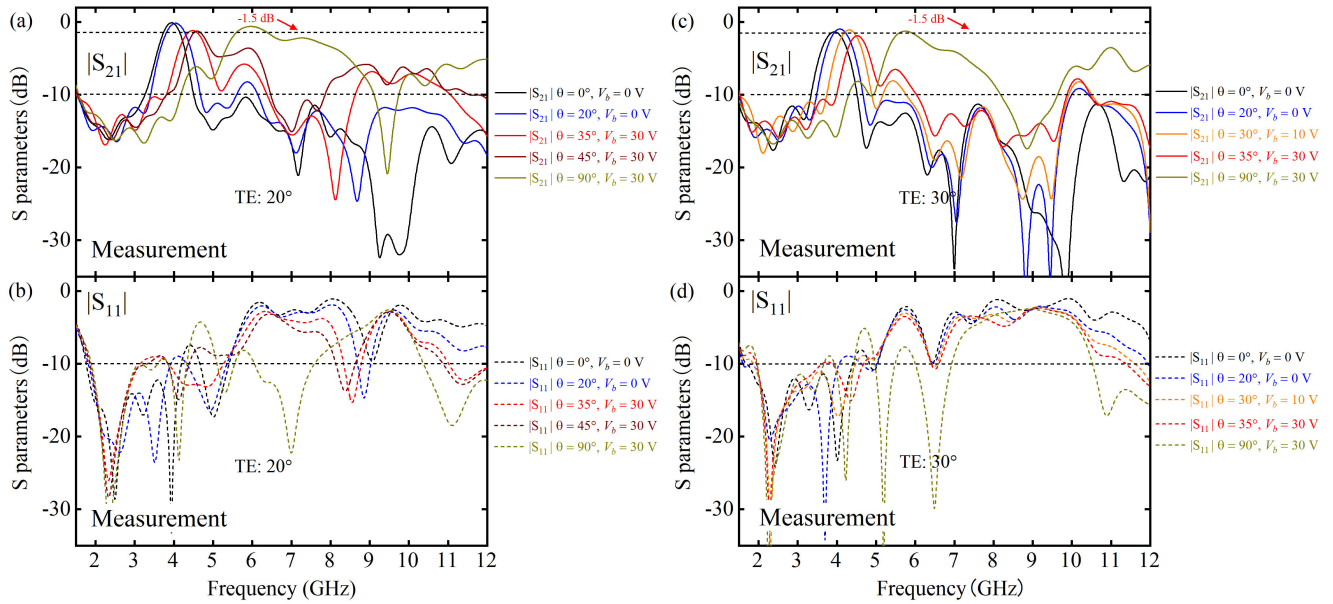

FIGURE 26. Measured S parameters of proposed rasorber under TE oblique incidence. (a) and (b): 20°; (c) and (d): 30°.

TABLE 2. Measurement result comparisons.

Reference	Polarization	Max. Absorption Band(s)	Transmission Frequency Covered (i.e. $\|S_{21}\| \geq -1.5$ dB)	No. of Transmission Band(s)
[30]	Dual	1.85∼2.52 GHz (30.66%) 4.00∼5.55 GHz (32.46%)	NA	Single
[31]	Single	2.20∼3.74 GHz (51.85%) 6.06∼6.75 GHz (10.77%)	4.50∼5.39 GHz (18.00%)	Single
[32]	Dual	4.7∼12.1 GHz (88.09%)	3.76∼3.95 GHz (4.9%) 7.58∼8.22 GHz (8.1%) 12.83∼14.72 GHz (13.7%)	Single
This Work	Single	1.8∼3.25 GHz (57.4%) 4.63∼5.8 GHz (22.4%) 10.05∼10.9 GHz (8.1%)	3.68∼4.77 GHz (25.8%) 5.99∼6.4 GHz (6.6%) 6.85∼7.84 GHz (13.5%) 8.52∼10.2 GHz (18.0%)	Single & Dual & Triple

outperforms the other counterparts in terms of the overall fractional transmission frequency range (63.9% vs. 26.7% in [30]), demonstrating excellent frequency reconfigurability of the proposed rasorber while maintaining a wide absorption bandwidth.

B. OBLIQUE INCIDENCE

To illustrate the device performance under oblique incident waves, the proposed rasorber is investigated experimentally under TM- and TE-polarized waves, as shown in Fig. 23, for various incident angles. As can be seen from the measured S parameters for TM-polarization under incident angles of $\pm 15°$ and $\pm 30°$ presented in Fig. 24 and 25, the rasorber is insensitive to the sign of incident angle. In addition, the device exhibits stable transmission and absorption performance at frequencies below 6 GHz while the lowest and highest transmission bands for $\theta = 90°$ and $V_b = 30$ V disappear under an incident angle of 30°. However, the device still exhibits an overall fractional transmission frequency range of 47.6%, far beyond that achieved in [32]. The absorption bandwidths of the proposed rasorber under 30° TM-polarized waves vary between 55.8% to 82.2%, demonstrating a slight degradation on the upper and lower bounds of absorption bandwidth.

Under TE-polarizations, the device demonstrates an overall transmission frequency range of 36.6% under an incident angle of 20°. Further increasing the incident angle to 30°, the transmission bands narrow to 20.1%. Hence, the device exhibits more serious performance degradation under TE-polarized oblique incidence compared with TM polarization. This is because the rasorber is a single-polarized device that can only operate properly under TM polarized waves. However, it seems the absorption performance is not significantly affected under TE-polarized oblique incidence. The measured fractional bandwidths, as shown in Fig. 26, are within 67.9% to 79.9%, with only a slight degradation compared with those measured under normal incident waves.

VI. CONCLUSION

This paper proposes a rasorber with reconfigurable transmission frequency combining both mechanical and electronic controlling mechanisms. The operation principles and equivalent circuit models of a mechanically reconfigurable FSS and electronically controlled resistive layer are analyzed. The rasorber can operate with single, dual and triple passbands with at least one absorption band and the device allows effective wave transmission within an overall fractional frequency range of 63.9% with a measured minimum insertion loss of 0.16 dB, outperforming those of any other existing reconfigurable rasorbers. The maximum fractional absorption bandwidth of the proposed device is comparable to the recorded maximum fractional absorption bandwidth of existing reconfigurable counterparts as well. Finally, the device is also experimentally investigated under oblique incidences, demonstrating excellent transmission and absorption performance up to an incident angle of 30° for TM-polarized waves. Due to the utilization of mechanically tunable frequency selective surface, the proposed reconfigurable rasorber may be used in applications where a relative slow responding speed is acceptable. In addition, the proposed reconfigurable rasorber also provides excellent flexibility for post-fabrication designs, which effectively improves its adaptability to the types of antenna and reduces the corresponding design and manufacturing cost. Therefore, the proposed reconfigurable rasorbers could potentially provide a low-cost design that suitable for the stealth application of multiple antennas.

REFERENCES

[1] B. A. Munk, *Metamaterials*. Hoboken, NJ, USA: Wiley, 2009. [Online]. Available: https://www.ebook.de/de/product/21140978/benedikt_a_munk_metamaterials.html

[2] A. Motevasselian and B. L. G. Jonsson, "Design of a wideband rasorber with a polarisation-sensitive transparent window," *IET Microw., Antennas Propag.*, vol. 6, no. 7, p. 747, 2012.

[3] F. Costa and A. Monorchio, "A frequency selective radome with wideband absorbing properties," *IEEE Trans. Antennas Propag.*, vol. 60, no. 6, pp. 2740–2747, Jun. 2012.

[4] X. Chen, Y. Li, Y. Fu, and N. Yuan, "Design and analysis of lumped resistor loaded metamaterial absorber with transmission band," *Opt. Exp.*, vol. 20, no. 27, p. 28347, Dec. 2012.

[5] Q. Chen, S. Yang, J. Bai, and Y. Fu, "Design of Absorptive/Transmissive frequency-selective surface based on parallel resonance," *IEEE Trans. Antennas Propag.*, vol. 65, no. 9, pp. 4897–4902, Sep. 2017.

[6] Z. Wang, Q. Zeng, J. Fu, W. Chen, B. Lv, M. Song, and T. A. Denidni, "A high-transmittance frequency-selective rasorber based on dipole arrays," *IEEE Access*, vol. 6, pp. 31367–31374, 2018.

[7] X. Xiu, W. Che, Y. Han, and W. Yang, "Low-profile dual-polarization frequency-selective rasorbers based on simple-structure lossy cross-frame elements," *IEEE Antennas Wireless Propag. Lett.*, vol. 17, no. 6, pp. 1002–1005, Jun. 2018.

[8] Z. Sun, J. Zhao, B. Zhu, T. Jiang, and Y. Feng, "Selective wave-transmitting electromagnetic absorber through composite metasurface," *AIP Adv.*, vol. 7, no. 11, Nov. 2017, Art. no. 115017.

[9] Z. Sun, Q. Chen, M. Guo, and Y. Fu, "Low-RCS reflectarray antenna based on frequency selective rasorber," *IEEE Antennas Wireless Propag. Lett.*, vol. 18, no. 4, pp. 693–697, Apr. 2019.

[10] M. Qu, S. Sun, L. Deng, and S. Li, "Design of a frequency-selective rasorber based on notch structure," *IEEE Access*, vol. 7, pp. 3704–3711, 2019.

[11] Q. Yu, S. Liu, A. Monorchio, X. Kong, Y. Wen, and Z. Huang, "A miniaturized high-selectivity frequency selective rasorber based on subwavelength resonance and interdigital resonator," *IEEE Antennas Wireless Propag. Lett.*, vol. 18, no. 9, pp. 1833–1837, Sep. 2019.

[12] Y. Han, W. Che, X. Xiu, W. Yang, and C. Christopoulos, "Switchable low-profile broadband frequency-selective Rasorber/Absorber based on slot arrays," *IEEE Trans. Antennas Propag.*, vol. 65, no. 12, pp. 6998–7008, Dec. 2017.

[13] Q. Chen, D. Sang, M. Guo, and Y. Fu, "Frequency-selective rasorber with interabsorption band transparent window and interdigital resonator," *IEEE Trans. Antennas Propag.*, vol. 66, no. 8, pp. 4105–4114, Aug. 2018.

[14] Z. Sun, Q. Chen, M. Guo, H. Yu, and Y. Fu, "Frequency selective rasorber and reflector with two-sided absorption bands," *IEEE Access*, vol. 7, pp. 6025–6031, 2019.

[15] X. Xiu, W. Che, W. Yang, Y. Han, and Q. Xue, "A highly selective rasorber based on second-order resonance," *IEEE Antennas Wireless Propag. Lett.*, vol. 19, no. 2, pp. 223–227, Feb. 2020.

[16] Y. Shang, Z. Shen, and S. Xiao, "Frequency-selective rasorber based on square-loop and cross-dipole arrays," *IEEE Trans. Antennas Propag.*, vol. 62, no. 11, pp. 5581–5589, Nov. 2014.

[17] X. Zhang, W. Wu, Y. Ma, C. Wang, C. Li, and N. Yuan, "Design dual-polarization frequency selective rasorber using split ring resonators," *IEEE Access*, vol. 7, pp. 101139–101146, 2019.

[18] Z. Shen, J. Wang, and B. Li, "3-D frequency selective rasorber: Concept, analysis, and design," *IEEE Trans. Microw. Theory Techn.*, vol. 64, no. 10, pp. 3087–3096, Oct. 2016.

[19] A. A. Omar, Z. Shen, and H. Huang, "Absorptive frequency-selective reflection and transmission structures," *IEEE Trans. Antennas Propag.*, vol. 65, no. 11, pp. 6173–6178, Nov. 2017.

[20] Y. Yu, G. Q. Luo, Q. Liu, W. Yu, H. Jin, Z. Liao, and Z. Shen, "3D band-absorptive frequency selective rasorber: Concept and analysis," *IEEE Access*, vol. 7, pp. 2520–2528, 2019.

[21] Y. Zhang, B. Li, L. Zhu, Y. Tang, Y. Chang, and Y. Bo, "Frequency selective rasorber with low insertion loss and dual-band absorptions using planar slotline structures," *IEEE Antennas Wireless Propag. Lett.*, vol. 17, no. 4, pp. 633–636, Apr. 2018.

[22] T. Deng, Y. Yu, Z. Shen, and Z. N. Chen, "Design of 3-D multilayer ferrite-loaded frequency-selective rasorbers with wide absorption bands," *IEEE Trans. Microw. Theory Techn.*, vol. 67, no. 1, pp. 108–117, Jan. 2019.

[23] X. Wang, M. Yan, Y. Fan, X. Fu, S. Qu, J. Wang, Y. Li, H. Chen, W. Chen, Q. Yuan, and H. Ma, "Transmission–absorption integrated structure via dispersion engineering of spoof surface plasmon polariton and frequency-selective surface," *J. Phys. D, Appl. Phys.*, vol. 53, no. 8, Dec. 2019, Art. no. 085001.

[24] C. Wang, Y. Li, M. Feng, J. Wang, H. Ma, J. Zhang, and S. Qu, "Absorption-transmission-integrated frequency selective structure based on spoof surface plasmon polariton modes," *J. Phys. D, Appl. Phys.*, vol. 52, no. 15, Feb. 2019, Art. no. 155103.

[25] L. Wang, S. Liu, X. Kong, H. Zhang, Q. Yu, and Y. Wen, "Frequency-selective rasorber with a wide high-transmission passband based on multiple coplanar parallel resonances," *IEEE Antennas Wireless Propag. Lett.*, vol. 19, no. 2, pp. 337–340, Feb. 2020.

[26] M. Guo, Q. Chen, Z. Sun, D. Sang, and Y. Fu, "Design of dual-band frequency-selective rasorber," *IEEE Antennas Wireless Propag. Lett.*, vol. 18, no. 5, pp. 841–845, May 2019.

[27] M. Guo, Q. Chen, D. Sang, Y. Zheng, and Y. Fu, "Dual-polarized dual-band frequency selective rasorber with low insertion loss," *IEEE Antennas Wireless Propag. Lett.*, vol. 19, no. 1, pp. 148–152, Jan. 2020.

[28] M. Guo, Q. Chen, T. Bai, K. Wei, and Y. Fu, "Wide transmission band frequency-selective rasorber based on convoluted resonator," *IEEE Antennas Wireless Propag. Lett.*, vol. 19, no. 5, pp. 846–850, May 2020.

[29] G. Qian, J. Zhao, X. Ren, K. Chen, T. Jiang, Y. Feng, and Y. Liu, "Switchable broadband dual-polarized frequency-selective Rasorber/Absorber," *IEEE Antennas Wireless Propag. Lett.*, vol. 18, no. 12, pp. 2508–2512, Dec. 2019.

[30] L. Wu, S. Zhong, J. Huang, and T. Liu, "Broadband frequency-selective rasorber with varactor-tunable interabsorption band transmission window," *IEEE Trans. Antennas Propag.*, vol. 67, no. 9, pp. 6039–6050, Sep. 2019.

[31] Y. Wang, S.-S. Qi, Z. Shen, and W. Wu, "Tunable frequency-selective rasorber based on varactor-embedded square-loop array," *IEEE Access*, vol. 7, pp. 115552–115559, 2019.

[32] S. C. Bakshi, D. Mitra, and F. L. Teixeira, "FSS-Based fully reconfigurable rasorber with enhanced absorption bandwidth and simplified bias network," *IEEE Trans. Antennas Propag.*, vol. 68, no. 11, pp. 7370–7381, Nov. 2020.
[33] D. Ferreira, I. Cuinas, R. F. S. Caldeirinha, and T. R. Fernandes, "3-D mechanically tunable square slot FSS," *IEEE Trans. Antennas Propag.*, vol. 65, no. 1, pp. 242–250, Jan. 2017.
[34] N. Marcuvitz, *Waveguide Handbook*. Peter Peregrinus Ltd, 1986.
[35] Y. Xiang, "The electrostatic capacitance of an inclined plate capacitor," *J. Electrostatics*, vol. 64, no. 1, pp. 29–34, Jan. 2006.

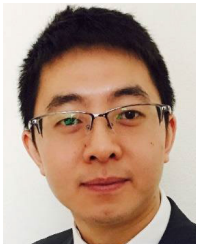

JING TIAN received the M.S. degree in electrical engineering from the Tampere University of Technology, Finland, and the Ph.D. degree in electronic engineering from the Queen Mary University of London, U.K. He is currently a Lecturer with the University of Electronic Science and Technology of China (UESTC). His research interests include electromagnetic metamaterials, graphene, and liquid crystal, based on EM devices.

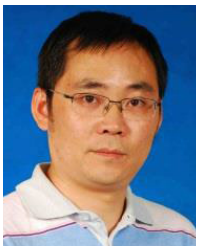

BO CHEN (Member, IEEE) received the B.S. degree from the University of Electronic Science and Technology of China (UESTC). He is currently an Associate Professor with UESTC. His research interests include microwave and millimeter wave measurement, antenna design, and electromagnetic compatibility and protection.

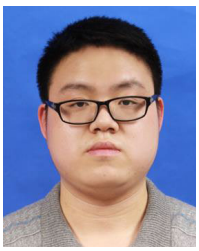

BIXIAO JIANG received the B.S. and M.Sc. degrees in electromagnetic field and wireless technique from the University of Electronic Science and Technology of China, Chengdu, China, in 2016 and 2019, respectively, where he is currently pursuing the Ph.D. degree in electronic and communication engineering. His research interests include electromagnetic metasurfaces design and electromagnetic scattering of plasma.

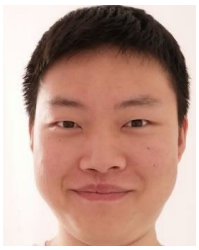

RUIMING LI (Student Member, IEEE) received the B.S. degree in electronic engineering from the University of Electronic Science and Technology of China (UESTC), Chengdu, China, in 2015, where he is currently pursuing the Ph.D. degree in electromagnetic field and microwave technology. His research interests include frequency selective surface and vortex electromagnetic wave imaging.

SHIWEN LEI (Member, IEEE) received the M.S. degree in communication and information systems from the Nanjing Research Institute of Electronic Technology (NRIET), Nanjing, China, in 2010, and the Ph.D. degree in signal and information processing from the University of Electronic Science and Technology of China (UESTC), Chengdu, China, 2015. From September 2015 to August 2017, he held a postdoctoral position with Lund University. He is currently working as a Senior Researcher with the School of Electronic Science and Technology, UESTC.

HAOQUAN HU received the B.S. and M.S. degrees in electronic engineering from the University of Electronic Science and Technology of China (UESTC). He is currently a Professor with UESTC. His research interests include antenna design and electromagnetic compatibility and protection.